SINET: Ethiop. J. Sci., 22(2):151–174, 1999
© Faculty of Science, Addis Ababa University, 1999 ISSN: 0379-2897

LITHOLOGIC AND STRUCTURAL MAPPING OF THE NORTHEAST LAKE ZIWAY AREA, ETHIOPIAN RIFT, WITH THE HELP OF LANDSAT TM DATA

Tesfaye Korme

Department of Geology and Geophysics, Faculty of Science
Addis Ababa University, PO Box 1176 Addis Ababa, Ethiopia

ABSTRACT: By integrating the interpretation of interactively enhanced Landsat Thematic Mapper (TM) image with field data it was possible to map the lithology and structures of the area located in the central part of the Main Ethiopian Rift (MER). Most lithologic contacts, faults and lineaments that were not identified in previous geological and structural maps of the region are mapped with better accuracy, minimum cost and shorter field season. Different image enhancement techniques were applied to enhance the original data. The resultant image is interpreted visually. The results of the work showed four major volcanic rock units, namely: 1. the lower series of pyroclastic deposit, 2. the basaltic series, 3. pyroclastic deposits of the rift floor and 4. recent lava flows. Three sets of faults were also mapped; 1. NE-SW striking rift-margin faults, 2. NW-SE to NNW-SSE trending trans-rift faults and lineaments and 3. the youngest and active NNE-SSW to N-S faults of the Wonji Fault Belt (WFB).

Key words/phrases: Ethiopia, fault, landsat TM, lithology, rift, volcanism

INTRODUCTION

Due to its rough topography, poor accessibility and other factors, large part of the resourceful land of Ethiopia has remained geologically unexplored. To overcome some of these barriers and unravel the resource potential of the country, the importance of integrating multi-source data such as remote sensing with that of conventional method field geological mapping is unquestionable.

Prior to the availability of satellite imageries, geologists relied on aerial photographs to obtain synoptic coverage of a study area. However, geologic interpretation of aerial photos is limited by many factors including poor spectral resolution, higher geometrical distortion, large number of photos required to recognise large surface features and higher cost (Rothery, 1984). Landsat TM data overcomes such handicaps in geological mapping and also provides the possibility of further treatment of the data in such a way that it fulfils the required sense of interpretation.

The objective of this study is therefore, to show how remote sensing data and methods of image interpretation improve the conventional methods of geological mapping, and to test some of the digital image processing techniques suggested for geological applications. Mapping structures in the inaccessible parts of the region and reconstructing the possible tectonic relationships among the faults of different phases and volcanism are the final results of this study.

LOCATION AND ACCESSIBILITY

The study area is located about 140 km south of Addis Ababa in the central part of the Main Ethiopian Rift (MER). It lies within 38°45' and 39°15'E. longitude and 8°00' and 8°15'N. latitude, covering about 1250 km^2 area (Fig. 1).

The topography of the central part of the MER is characterised by intensively faulted blocks with steep scarps forming local horst and graben structures. Long and relatively narrow (1–5 m) extension fractures (Tesfaye Korme *et al.*, 1997), brecciated lava flows, lava domes, cinder cones, craters and calderas are the most notable features within the study area. These features produced extremely rough topography. Due to such rough topography and absence of routes, accessibility to some localities in the area is rather difficult. There is only one dry weather road joining Asela and Meki towns. This road helped to accede at some of the representative geologic sections which were used as test areas while mapping the lithology of the inaccessible zones applying techniques of remote sensing.

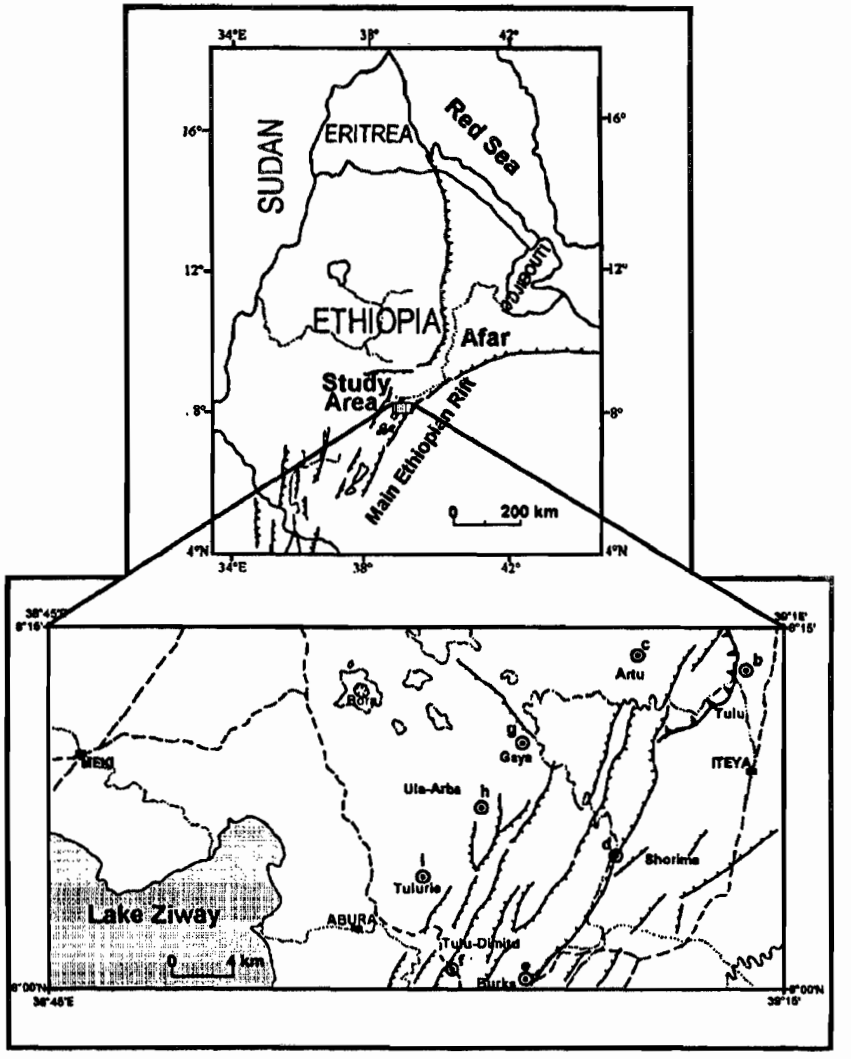

Fig. 1. Location map of the study area. Circles with dot at the centre show location of stratigraphic columns, broken lines with dot are contours, dotted lines are rivers and dashed lines are all weather roads.

GEOLOGY OF THE ETHIOPIAN RIFT

The MER is part of the great East African rift and lies within 5°00' and 9°00'N. latitude and 37°30' and 40°00'E. longitude (Mohr, 1967b). The Main Ethiopian Rift is geographically divided into three sub-sectors: Northern, Central and Southern sectors (Gidey Wolde-Gabriel *et al.*, 1990). Its geometry is characterised mainly by normal step faults of various dimensions with orientations ranging from NNE-SSW to NW-SE (Mohr, 1967b; Di Paola, 1977). These faults are commonly arranged in side-stepping an en-echelon style. The adjacent plateaux on the either side of the rift are formed by huge piles of Tertiary basaltic and rhyolitic lava and a number of Tertiary shield volcanoes. However, there are also windows of metamorphic basement rocks of Precambrian age and Mesozoic sedimentary rocks in a few localities. These pre-Tertiary rocks are exposed along the eastern, western and southern Afar margins (Huchinson and Engels, 1970; Zanettin and Justin-Visentin, 1974; Black *et al.*, 1975; Chessex *et al.*, 1975). They also occur along the western margin of the central sector of the MER at Kella Horst, and at Amaro Horst in the southern sector of the MER (Levitte *et al.*, 1974; Zanettin *et al.*, 1980). In the southern sector of the MER, crystalline basement is unconformably overlain by various Tertiary (12.7–49.4 Ma) and quaternary volcanic rocks, including the oldest known (Eocene) flood basalt in Ethiopia (Davidson and Rex, 1980). The floor of the Ethiopian Rift is in general covered by Mio-Pliocene to present volcanics and volcano-sedimentary deposits.

LANDSAT TM DIGITAL IMAGE PROCESSING, INTERPRETATION AND GEOLOGICAL MAPPING

Digital data and the software

The study area lies within a scene of LANDSAT-5 Path-168 and Raw-54 taken on November 22, 1989. A window of 1950 columns and 1289 lines containing four TM bands was extracted and treated using ERDAS software installed on PC. Further treatments were also made on an APOLLO station with TGV software which is developed locally at the University of Pierre and Marie Curie, Laboratory of Remote Sensing.

Image processing includes mathematical manipulations on raw digital data that enables us to get images containing more information that are essential for the

final goal of the work. In this study, image processing was carried out with some information from the existing geological map at 1:250,000 scale and additional geological data from reconnaissance field work. The bands available were TM band2, band3, band4 and band5 (while TM band1, band6 and band7 are lacking). Various methods and processing techniques were applied to enhance the images and compensate for the lack of information from TM band7. Band rationing, principal component analysis and spatial filtering were among the principal mathematical manipulations applied on the four bands to extract the maximum possible information which are required for geological mapping.

Digital data processing

a. Colour combinations

Covariance matrix is calculated (Table 1) to investigate the distribution of information among the four bands. The matrix indicates the joint variance (co-variance) between bands about their weighted mean. When the co-variance between two bands is positive, the information in the bands are positively correlated, and hence there is high redundancy. If it is negative, an inverse relationship exists, and consequently, features represented by higher digital number values (brighter pixels) in one of the bands will have lower values (darker pixels) in the other band. If co-variance is zero, then the information contained in the two bands are independent. Co-variance matrix also helps in selecting bands for colour combinations. According to the covariance matrix of the data used in this study (Table 1), there is relatively higher redundancy of information among the bands used except for band3, band4, and band5. Thus, a good colour combination image showing diverse surface covers (e.g., rocks, soil and vegetation) is obtained by composing the TM bands 5, 4 and 3 in red, green and blue (RGB) order.

Table 1. Covariance matrix of the four bands.

Bands	B2	B3	B4	B5
B2	719.4			
B3	159.5	58.72		
B4	309.5	**112.8**	223.3	
B5	207.4	**70.34**	**135.4**	173.8

b. Principal component analysis

Principal component analysis is a mathematical method of improving the spread of data about a new set of axes in multi-dimensional space (Drury, 1992). It avoids redundancy of information in different bands. In the case of the data used in this study, the original bands (band2, 3, 4 and 5) are projected onto four new principal axes as linear additive combinations using calculated eigen vectors (Table 2). Each eigen vector is a loading factor for the contribution of individual band to a principal component. The co-variance matrix of the original bands is transformed in such a way that the new co-variance between the transformed canals (principal components) becomes zero. This means that, there is no more redundancy among the transformed canals. Variations within information contained in individual transformed canals are recognised as eigenvalues which are considered as variances of the principal components (Table 3).

Table 2. Eigen vectors and calculated principal components of the four bands.

Band	B2	B3	B4	B5					
PC1	0.83	0.21	0.42	0.00	⇒	PC1 =	$0.83B_2$	$+0.21B_3$	$+0.42B_4$	$+ 0B_5$
PC2	-0.53	0.22	0.43	0.90	⇒	PC2 =	$-0.53B_2$	$+0.22B_3$	$+0.43B_4$	$+0.90B_5$
PC3	-0.18	0.31	0.67	-0.65	⇒	PC3 =	$-0.18B_2$	$+0.31B_3$	$+0.67B_4$	$-0.65B_5$
PC4	0.00	0.90	-0.44	-0.02	⇒	PC4 =	$0B_2$	$+0.90B_3$	$-0.44B_4$	$-0.02B_5$

The highest eigenvalue corresponds to the first principal component and, the values decrease rapidly towards the higher order principal components (Table 3). The result is that, the first principal component is generally a weighted average of all of the data and approximates an image of albedo and topography in the range covered by remote sensing systems (Drury, 1992). High order principal components contain detailed information concerning the different types of lithologic and vegetation covers of the area. By applying directional and edge enhancement filters on the first principal component image we have obtained large number of fault zones and other lineaments in a preferred direction, well defined lithologic boundaries and other land-cover limits.

Table 3. Eigenvalues.

Neocanals (PC)	Eigen values	Variance (%)	Cumulative variance (%)
PC1	991.83	84.41	84.41
PC2	122.58	10.43	94.84
PC3	59.06	5.03	99.87
PC4	1.52	0.13	100.00

c. Band rationing

The ratio images have the effect of suppressing unnecessarily detailed spectral responses which are introduced due to rough topography, while better enhancing the colour boundaries. Therefore, they are very useful in lithological mapping since they directly exaggerate subtle colour differences among the different rocks exposed on the surface. Many geological problems such as tracing lateral facies variations require fine lithologic mapping. For such type of mapping ratio images derived from infrared and visible bands gives better result than detailed field mapping. However, rationing reduces the ability to discriminate between two rocks with very different albedos, but similar spectral reflectance (Drury, 1992).

The ratio image used in this study is computed with the formula indicated below from TM band3 and band5 which are the least correlated bands (Table 1). After rescaling its dynamic range between 0 and 255, the ratio image is found to be rich in information that are useful for lithologic mapping.

$$Ratio\ image = Band5 - \frac{Band5 - Band3}{Band5 + Band3}(K)$$

where, k is a constant for re-scaling the dynamic of the resultant image.

d. Edge enhancement and linear directional filtering

Edge enhancement and linear directional filtering are particularly important in smoothening images, in enhancing certain lineaments of preferred orientations and in detecting lines and edges such as lithologic contacts and lava flow structures. They are also used to reduce the effect of differences in illumination over the area.

A consequent limitation of filters, mainly the high pass ones, is that, only local variations with respect to neighbouring pixels become important and the absolute DN-values have no significance in image interpretation (Gupta, 1991). The image used in structural mapping of the study area is obtained by applying first, a high-pass NE-SW directional filter of (7 x 7) to the TM band 4 and, then adding the filtered image to the original. This process has strongly modified the individual pixel values near the edges and lines that are enhanced. It has largely enhanced the visibility of the NW-SE to NNW-SSE striking trans-rift faults and lineaments which will be discussed in the structural mapping section of this manuscript.

e. Geometric correction

Like any other Satellite data, the geometric distortion associated to Landsat TM data requires correction. Due to relatively unstable mechanical scanning system of the Landsat TM sensor, the associated geometrical distortion in TM images is irregular and it can not be easily modelled like that of SPOT images (Story and Congalton, 1986). However, the geometric correction of images used in this study is done with respect to a Universal Transverse Mercator (UTM) topo-map of 1:50,000 scale. To perform this correction, 33 ground control points (GCP) which are uniformly distributed in the image have been carefully selected on both the image and the reference topo-map. The first calculation of geometric correction is done with the first order transformation at total root mean square (RMS) error of 2.5. The result obtained after iteration indicated that about half of the total GCP have been correctly identified at RMS of 2.5. However, the maximum acceptable total RMS error for good geometric correction is 2.0. Therefore, it is necessary to reduce the RMS error as lower as possible keeping the maximum number of GCP (Tables 4 and 5). At the total RMS error = 1.43398 seven ground control points are accepted. These seven ground control points are sufficient to correct the geometry of the image at the required scale.

The DN-values of the raw image are interpolated to the new geometrically corrected grid using the method of bicubic interpolation. This method uses a polynomial surface to fit the DN values into the new grid. Hence, the resultant image is not only corrected geometrically, but also modified radiometrically (Gupta, 1991), and it has identical projection and scale to the referenced UTM topo-map of scale 1:50,000.

Table 4. Ground control points (GCP) after iteration at RMS = 1.43398

Ground control point (GCP) number	Co-ordinates on topo-map (UTM)		Co-ordinates on image (pixels)	
	Latitude	Longitude	X	Y
2nd	476015.0000	892075.0000	252	987
4th	489087.0000	896045.0000	707	797
8th	478050.0000	908080.0000	252	415
17th	506055.0000	903053.0000	1255	456
20th	501053.0000	887075.0000	1078	832
26th	524055.0000	894040.0000	1927	681
33rd	511060.0000	881060.0000	1527	1197

Table 5. Errors contributed by the ground points.

Ground control point (GCP) number	Total error	Error contributed by the GCP
2nd	1.5506	1.0813
4th	1.6232	1.1319
8th	1.6958	1.1826
17th	1.4915	1.0401
20th	1.1640	0.8118
26th	0.9814	0.6844
33rd	1.3467	0.9392

Image interpretation and geological mapping

In remote sensing application to geologic mapping, the most important task that follows image processing is the interpretation. Even though it is possible to identify and classify the different themes in the image automatically, more accurate result is obtained by visually interpreting the images. In this study, interpretation is done on a 1:100,000 scaled printed image and at a screen having higher resolution contemporaneously. This interactive interpretation permits to zoom the digital image where detailed interpretation is required.

Using the colour combination image of TM band5, ratio of band5 and band3 and principal component 2 in RGB order, nine different themes were identified of which seven of them represent the different rock units (Fig. 2). The geological map shown in Figure 3 is a result of compilation by integrating image interpretation with field geological data. The spectral separation among the different themes in each transformed (neocanals) and original bands indicated in Figure 2 confirms that, TM band5, ratio image, and PC1 and PC2 contain the DN values characterising the themes established.

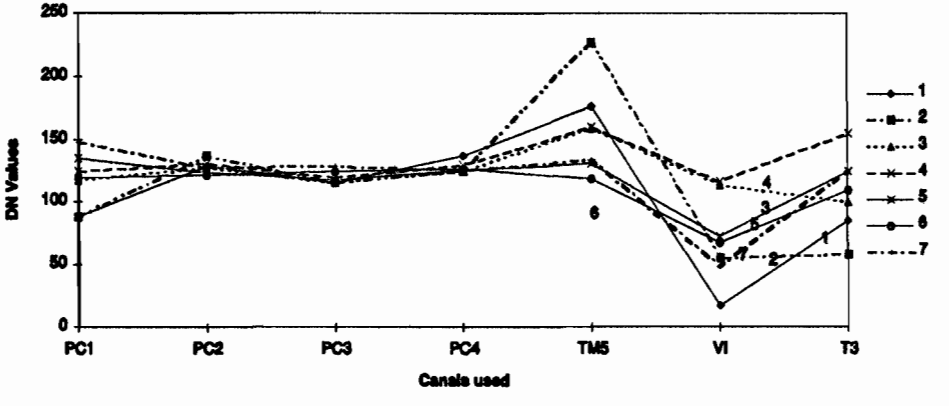

Fig. 2. **Scaterogram showing the separation of different themes among the canals used.** PC, principal component image; TM5, TM band5 original image; VI, Vegetation index (band ratio) image; and T3, Texture image derived by applying texture filter on TM band3. Themes: 1. Rift margin pyroclastic deposits, 2. Porphyritc olivine basalt, 3. Trachytic rocks, 4. Rift floor pyroclastic deposits, 5. Rift floor scoriaceous porphy. basalt, 6. Obsidian flows forming lava domes and 7. Very recent scoriaceous basalt.

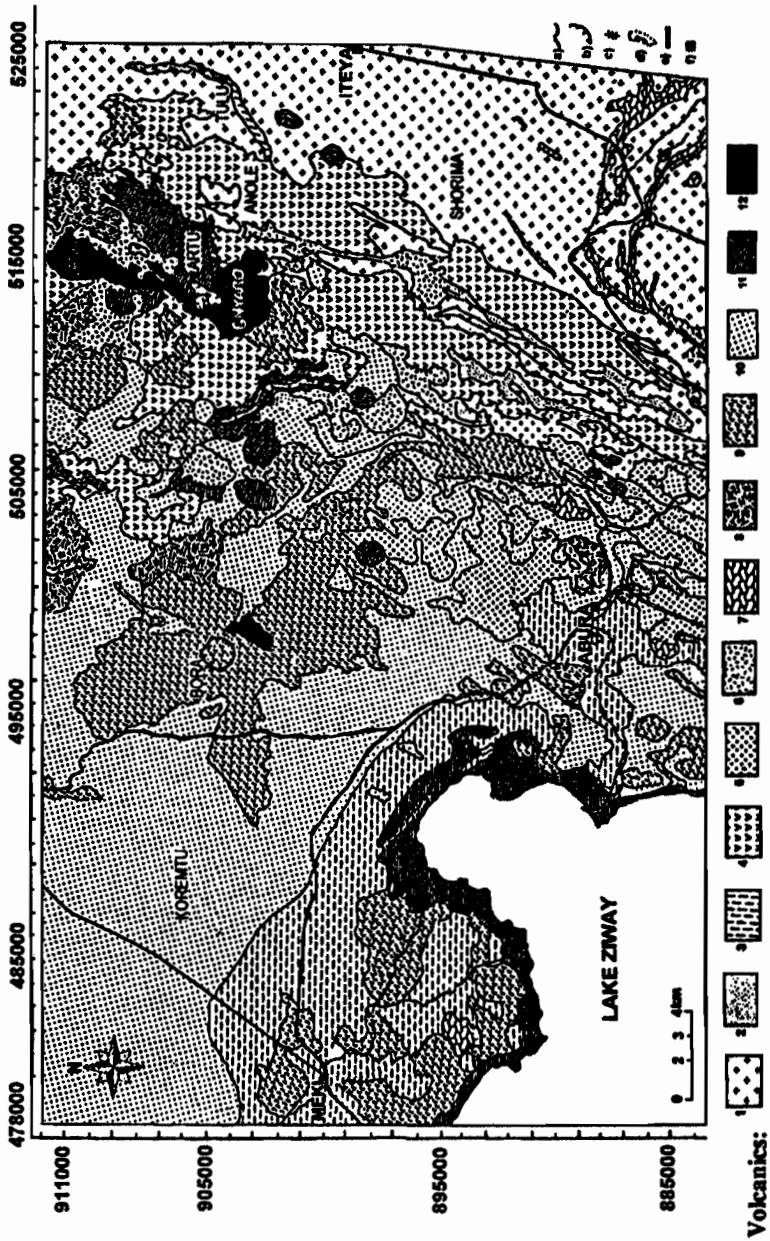

Fig. 3. Geological map of Northeast Lake Ziway area as interpreted from Landsat TM images. Lithologic contacts that were not identified on satellite image are mapped during the field verification stage. (1, Rift margin pyroclastic deposits; 2, Ash falls and ignimbrites; 3, Co-ignimbrite breccia and caldera-rim rock suit; 4, Porphyritic olivine-plagioclase basalt; 5, Olivine basalt; 6, Scoriaceous porphyritic basalt; 7, Rhyolitic lava and sheeted ignimbrites; 8, Trachytes; 9, Rift floor pumice dominated pyroclastic flows; 10, Rift floor ash dominated pyroclastic fall and alluvial deposits; 11, Rift floor scoriaceous basaltic flows and cones; 12, Obsidian flows and domes; 13, Sand and silt deposits; and 14, Mud. a, Lithologic contacts; b, Calders; c, Socoria and tuff cones; d, Volcanic craters; e, All weather roads; f, Towns.)

Geological units

The seven geological units which are represented by the different themes are shown on Figure 2. Their field and petrographic characteristics are outlined in the following section.

1. Rift margin pyroclastic deposits

This unit comprises pumiceous ignimbrites, ignimbrites with fiamme, tuffs, highly weathered rhyolitic flows and extensive pumice and ash fall deposits. Field observation shows that the lower part of the unit is characterised by welded ignimbrite which contains numerous lithic fragments in it. The overall thickness of this ignimbrite is about 50 m in Wedecha river valley, 10 km east of Iteya town (in Fig. 4-a). In this area, it is intercalated with thin layers of ash fall. Between the lower ignimbritic unit and the upper pyroclastic fall, there is a paleosoil horizon of 30 to 50 cm thick. The pyroclastic fall is partly ejected from Tulu caldera which is about 8 km in diameter (Fig. 4). The flow products of this caldera are represented by local and poorly lithified co-ignimbrite breccia, 1.5 m thick highly welded ignimbrite containing significant amount of juvenile magma or fiamme (in Fig. 4-b). The co-ignimbrite breccia is mainly contains fragments of porphyritic basalt, scoria, rhyolite and few intrusive igneous rocks. The size of these fragments reaches up to 40 cm in diameter. The ignimbrite overlying the breccia contains fiammes that are being devitrified to chalcedony. Petrographically, the ignimbrite contains fractured crystals of anorthoclase and few aegirine augite. The groundmass is glassy and shows flow texture.

2. Porphyritic olivine basalt

It is the thickest and widely distributed basalt type in the area. It is about 13 m thick around Artu (in Fig. 4-c) and attains a maximum thickness of 15 m closer to the Anole village (Fig. 3). This basalt is of pahoehoe-type and outpoured through extension fissures (Tesfaye Korme *et al.*, 1997) located between Deneba (in the southern part of the study area) and Anole villages. It becomes aphyric closer to the top and has a 30 cm thick agglomerate layer that marks the contact between the porphyritic and the aphyric parts of the basalt. Stratigraphically, this basalt overlies the pyroclastic deposits of Tulu caldera with 30 cm thick paleosoil in between (in Fig. 4 - c and d). Petrographically, it is composed of abundant plagioclase crystal laths and very few pyroxene and

olivine along with highly altered titano-augite and rutile needles. The olivine phenocrysts are characterised by idingitization rims resulting from chemical alteration. Both the primary and secondary vesicles found at the surface of the porphyritic basalt are partly refilled by carbonate minerals and partly by clay minerals derived from alteration of the plagioclase and the ferromagnesian phenocrysts. The chemical alteration has affected homogeneity of the reflectance from total rock and resulted in a rough textured satellite image.

3. Trachytic rocks

The rocks that are spectrally categorised in this group are mainly greenish-grey ignimbrites and trachyte. They occur in the form of sheet flows, hemispherical (mushroom-shaped) lava domes, and cliffs forming caldera rims. Trachytic lava flow overlies the porphyritic olivine basalt around Artu (in Fig. 4-c). It abuts against the major fault scarps that cut the porphyritic olivine basalt. Hence, it is younger than the basalt and the major tectonic phase that has formed rift-in-rift structures of the rift floor.

The rock samples taken from the trachytic lava flow around Artu and Tirbocha (Fig. 3) contain substantial amounts of euhedral plagioclase and alkali feldspar phenocrysts and a few aegirin and magnetite crystals. Its groundmass is mainly composed of feldspar laths and relatively few quartz crystals. This dominance in feldspar over quartz proves that the rocks constituting the hemispherical lava domes in the area are mainly trachytic not rhyolitic in composition.

4. Rift floor pyroclastic flow and fall deposits

Rocks in this spectral category include sheeted pumiceous ignimbrites (Fig. 4 - e and f), pumice and ash deposits around Bora area (Fig. 3). It also contains recent alluvial and lacustrine deposits surrounding lake Ziway. The lacustrine deposit in the area is mainly composed of volcanoclastic materials. Major part of the rift floor pyroclastic flow and fall deposits are emitted from Bora and the surrounding volcanoes which mark a period of intensive acid volcanism in the rift. Angular obsidian rock fragments which are found in the pyroclastic fall deposits around Bora volcano are partly derived from brecciation of previously existing obsidian layer and partly from the chilling of acid magma due to direct contact with groundwater while ascending to the surface. The obsidian fragments formed by the later mechanism contain some phenocrysts of feldspar and quartz.

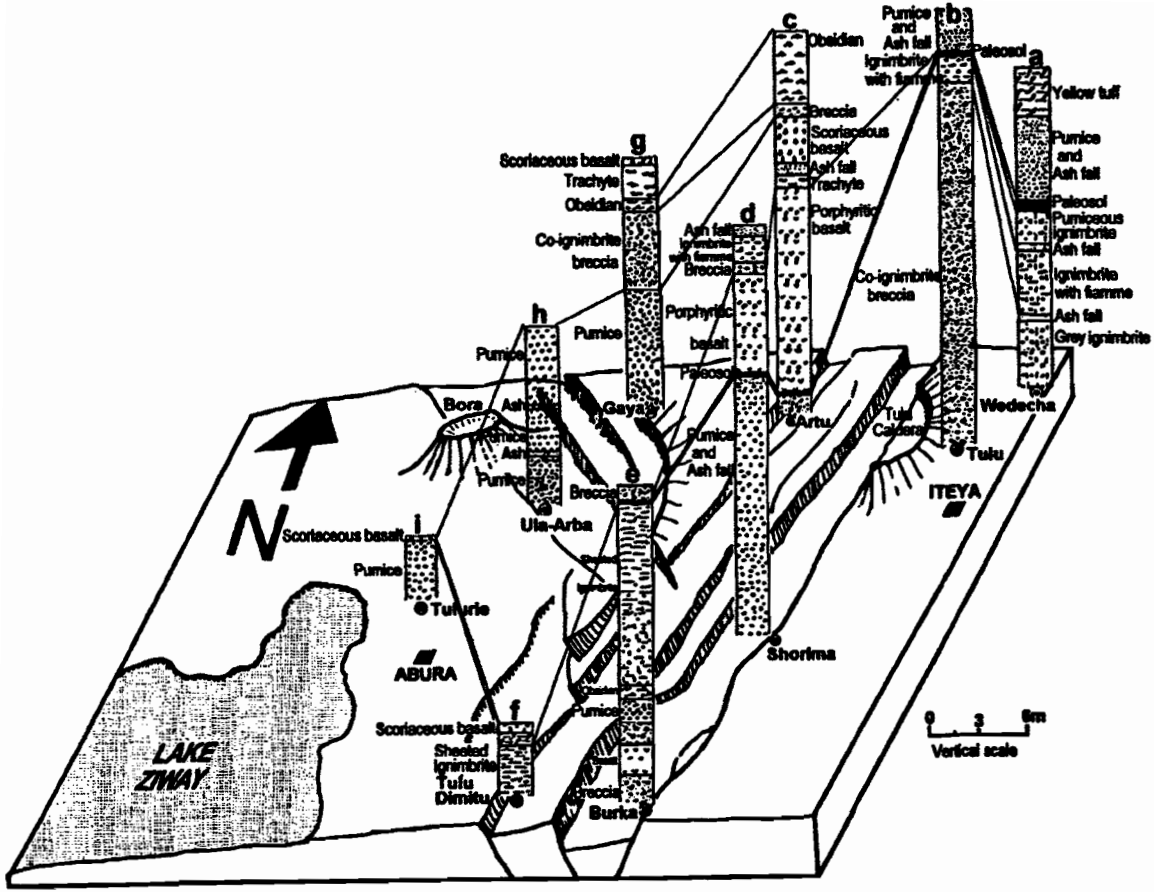

Fig. 4. Stratigraphic columns correlation for representative sections in the area. The locations of columns are indicated in Figure 1.

5. Rift floor Scoriaceous basalt

It is the youngest basalt that has outpoured through Recent NE trending open faults (Tesfaye Korme *et al.*, 1997) and related fractures of the WFB. It occupies the axial zone of the Rift floor, mainly in the form of aa-type, thin lava flow. Most of the fissures system through which the basalt has poured out are characterised by alignment of fumeroles showing the active nature of the latest phase of volcano-tectonic processes in the axial zone. The aerial distribution of this basalt is restricted to zones which are affected by intense rift parallel faults cut by NW-SE trending trans-rift faults. It also occurs in the form of lava domes, cinder cones and blister cones which are formed by accumulation of gases while cooling. Its flow pattern and lateral extent is largely controlled by the present topography of the rift floor and the NNE trending graben and horst structures. Petrographically, it contains crystal laths of plagioclase feldspars and opaque groundmass. The absence of ferromagnesian and plagioclase phenocrysts in considerable quantity from the basalt suggests that the basalt is a compositionally evolved or differentiated type.

6. Obsidian flows forming lava domes

This category includes all the varieties of glassy rocks such as obsidian, pitchstone, perlite and pumiceous glass and their weathered equivalents outcropped in Artu (in Fig. 4-c) and Gaya (in Fig. 4-g). They are mainly found along active fault zone through which they are emitted. The domes are generally hemispherical in shape, and show well preserved lava flow structures. They are also found as elongated ridges trending along the fractures through which they were extruded. The presence of phenocrysts of alkali feldspars and quartz crystals indicates that the obsidian is formed by the interaction of groundwater and compositionally evolved low temperature magma (Best, 1986).

7. Pumice and ash fall

This very thin pyroclastic fall unit blankets the top part of the volcanic rock succession in the area. It is found as alternating layers of well sorted pumice and ash falls (in Fig. 4-h). The sources of the fall deposits are the youngest tuff-rings found along the axial part of the Rift.

Stratigraphy

Stratigraphic columns loged from sections exposed at different parts of the region are shown on Figure 4. From these stratigraphic sections, it is clear that the aerial distribution and thickness of individual rock type is not uniform. In

many cases, however, a specific volcanic rock assemblage which characterises one phase of eruption is followed by paleosoil horizon indicating that each phase of volcanic eruption is separated from the other by considerable time gap. On the bases of compositional similarities and stratigraphic positions, the rocks in the area can be categorized into four major groups (Table 6).

Table 6. The four major groups of rocks in the study area.

Group	Major rock types included in the group	Common features and origin of the group
Fresh lava flows (youngest)	- Obsidian lava flow and dome - Scoriaceous (aa-type) basalt	Fresh lava flows emitted through open fractures belonging to the WFB
Pyroclastic deposits and acid lava flows	- Trachytic and rhyolitic rocks - Rift floor pyroclastics	Acid volcanic products emitted from volcanoes in the WFB zone
Porphyritic alkaline basalt	- Rift floor porphyritic. basalt - Eastern escarpment basalt	Highly porphyritic fissural basalt with larger phenocrysts of plagioclase and olivine
Pyroclastic flows and falls (oldest)	- Co-ignimbrite breccia and related ignimbrites - Main escarpment pyroclastics	Older and extensive pyroclastic products extruded through older fissures or calderas

The following attempts were made in order to put the major rock groups in the area in regional stratigraphic framework. The oldest pyroclastic flows and falls mapped in the area belong to the Nazareth Group of upper Miocene-lower Pliocene age which includes the eastern escarpment pyroclastic deposits (Morbidelli *et al.*, 1975; Juch, 1975; Kunz, *et al.*, 1975; Meyer *et al.*, 1975; Gidey Wolde-Gabriel *et al.*, 1991). Extensively outcropped porphyritic alkaline basalt is the equivalent of Chilalo basalt of middle to upper Pliocene age (Gidey Wolde-Gabriel *et al.*, 1991). The Chilalo series overlies the Nazareth Group pyroclastic deposits, and it includes silisic rocks and basaltic flows. The remaining two rock groups overlying the porphyritic basalt can be included in the Wonji Group (Mohr, 1967a). The Wonji group consists of diverse quaternary lava, pyroclastic deposits, and volcanoclastic debris younger than 1.6 m.y. which are generally confined to the WFB (Mohr, 1967b; Kazmin, 1979).

Geological structures:

The synoptic view of satellite images is ideal for mapping and analysing the regional pattern of systems of faults and other lineaments over larger areas (Gupta, 1977; Drury, 1992). Small, regionally insignificant features can be suppressed while very large and subtle features are clearly detected. From the interpretation of Landsat MSS band 7 image across the MER, it is observed that most of the rivers that drain down to the rift floor are mainly controlled by the NW-SE trending trans-rift faults and lineaments (Fig. 5) which were not identified neither on large scale aerial-photographs nor by field mapping. These lineaments are well mapped (Fig. 6) and analyzed in detail from directionally filtered Landsat TM band 4 image of the study area.

The normal faults in the area are not continuous; some of them die out in short distance and/ or continue propagating in an en echelon style. Sometimes, there develops a system of splay faults and tail cracks at their terminations. This pattern of propagation and splaying at their termination are indicators of the presence of associated strike-slip movements under NW-SE orientated maximum extension direction (Chorowicz *et al.*, 1994; Tesfaye Korme *et al.*, 1997). From directionally filtered Landsat TM image, aerial photo interpretations and field observation, three major groups of faults are identified: 1. NE-SW rift margin normal faults, 2. NW-SE trans-rift strike-slip faults and 3. NNE-SSW and N-S youngest normal faults (Fig. 6).

1. The oldest NE-SW faults found at the Northwest of Asela town have persistently similar direction with the eastern rift margin faults. They are younger than the Chilalo trachyte and basalt of middle to upper Pliocene age (Gidey Wolde-Gabriel *et al.*, 1990). These faults have their down throws NW-ward with magnitude up to 60 m.
2. One of the results of structural mapping using the satellite digital data obtained in this study is the detection of NNW-SSE to NW-SE right lateral strike-slip faults. From directionally filtered TM band4, the active strike-slip faults are identified in two different zones traversing the area. One of these zones starts far on the top of mount Chilalo (Fig. 5) and extends down to the rift floor passing through the northern boarder of lake Ziway and it extends up to the western rift margin (Figs 5 and 6). It mainly controls the courses of Ketar and Meki Rivers (Fig. 5). Some of the faults belonging to this group precede the major marginal faults, the others are after and the latest ones are even younger than the Wonji Fault belt. Because, at some localities these faults cut the NNE-SSW striking faults of the WFB, while in some localities outside the study area some of them are cut by the rift margin faults.

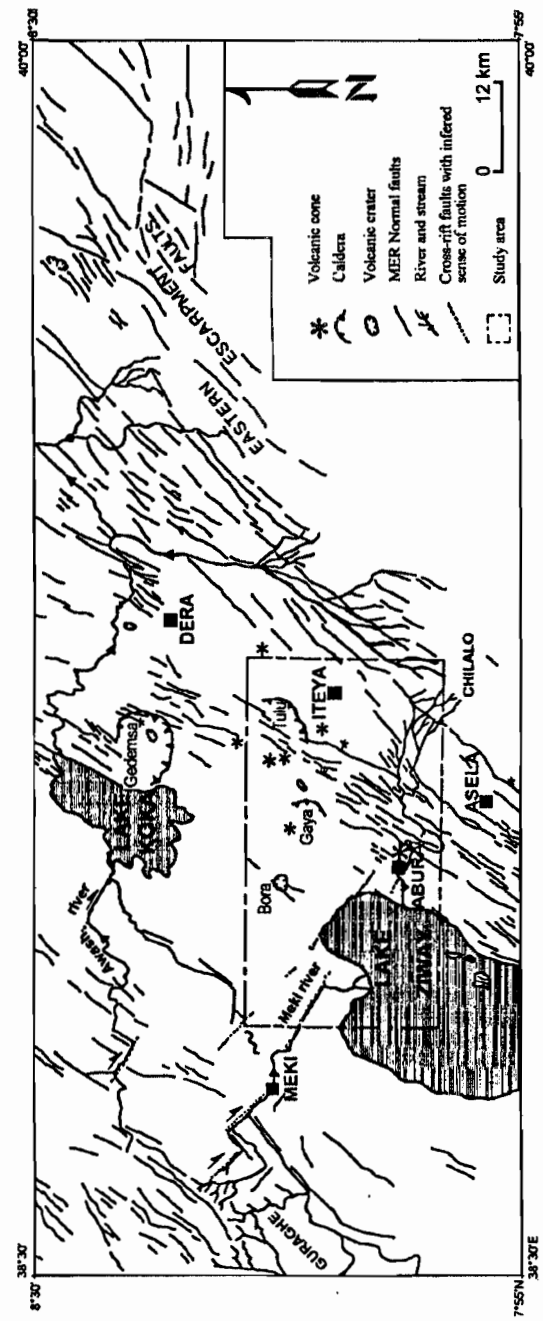

Fig. 5. Lineament (fault) map across the MER between 7°55'N and 8°30'N latitudes. It is interpreted from Landsat MSS band 7 image.

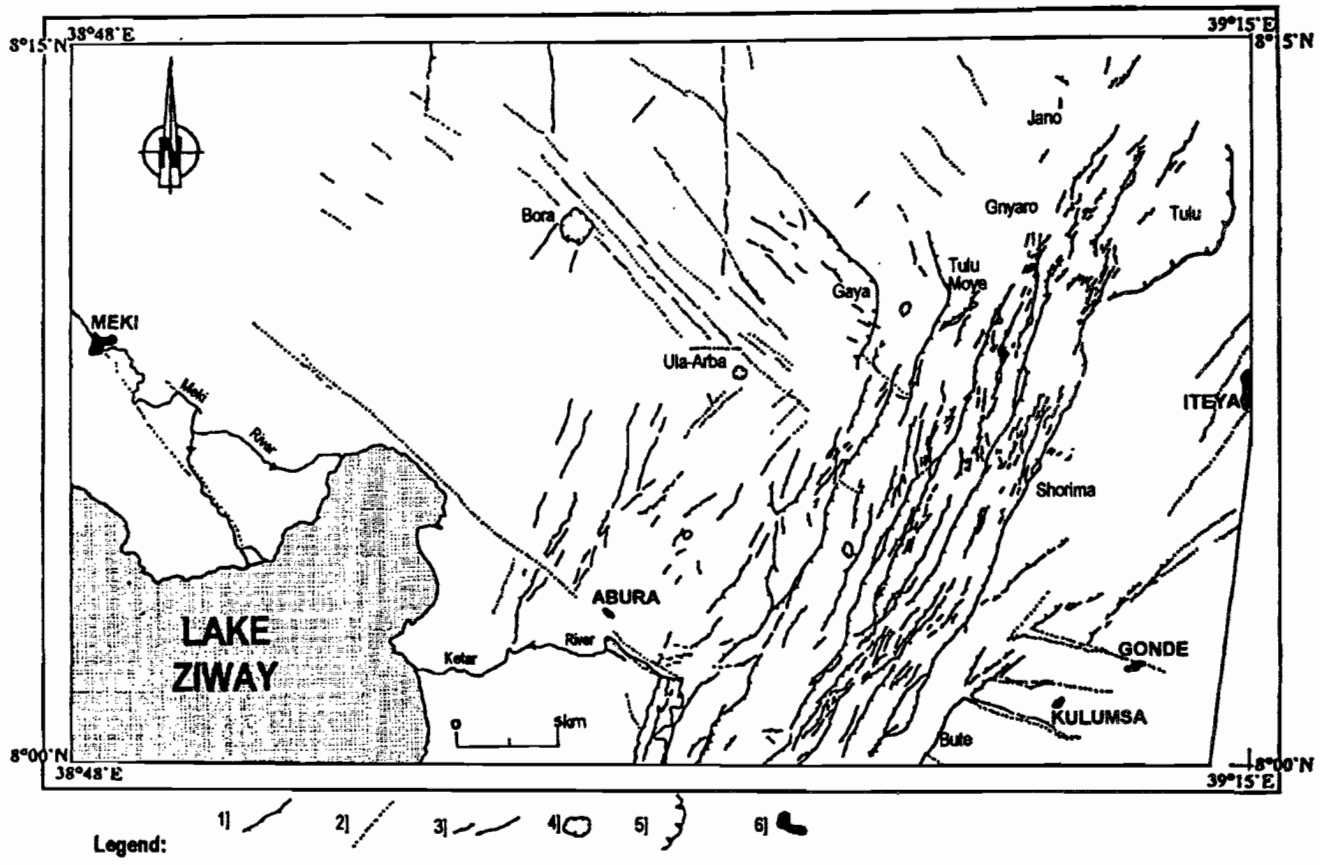

Fig. 6. Detailed tectonic map of Northeast Lake Ziway area. This map is compiled from the interpretation of directionally filtered Landsat TM band 4, aerial photographs and field mapping. 1, Normal fault; 2, Trans-rift faults and lineaments mapped from directionally filtered images; 3, Tension gashes and open faults; 4, Caldera; 5, Crater; and 6, Town.

The second location of zones affected by the NNW-SSE trending strike-slip faults in the area is west of Gaya caldera where it forms a discordant graben-like structure that crosses Ula-Arba area and Bora crater (Fig. 6). The discordant graben like structure is cut by the NNE-SSW striking WFB.

3. The youngest NNE-SSW to N-S trending faults of the Wonji Fault Belt found in the area are generally of scissors types normal faults with a small dextral component (Chorowicz *et al.*, 1994) and have throws up to 30 m to the west as well as to the east. They form rift-in-rift system which contains several narrow horst and grabens that run parallel to each other for tens of kilometres along the axis of the rift.

It is the most active system of fault which is thought to have been controlled by the pre-existing ancient weak zones in the underlying Precambrian and Mesozoic rocks (Smith and Mosely, 1993). NNE-SSW to NE-SW tension gashes of about two meters wide and hundreds of meters long without an appreciable vertical displacement are associated to this group of faults. Sometimes, these fissures are partly filled by basaltic lava and aligned geysers.

DISCUSSION

A simple dynamic stretching gives sufficiently interpretable images. However, to avoid the effects of shadow on the reflectance received from the west facing fault scarps and caldera and crater rims, the importance of successive advanced image processing is recommendable. The common enhancement techniques such as PCA, Band Ratio, Brightness Index and False Colour Compositions of raw and transformed canals are usually applied to enhance images for use in geological mapping. Edge enhancement and Laplacian filters are mainly used in mapping the lithologic contacts and linear structures, respectively. They are particularly useful in identifying the flow-structures typical of rhyolithic lava and mapping the NNW-SSE trending trans-rift faults and other lineaments.

Mapping of the normal faults facing the illumination direction from satellite raw data is more difficult than the opposite facing ones. This is because the opposite facing fault scarps are characterised by dark and linear bands or strips, while the illumination facing scarps have brighter and less contrasted strips that confuse with the reflectance received from some of the brighter rock types such

as ash and pumice deposits. Applying directional filters can minimise such confusion and aids in mapping other lineaments as well. Maximum attention has to be given in interpreting filtered images, because, errors may be introduced due to artifacts and the processing technique itself.

The geological map derived from visual interpretation of colour composition of TM band 5, PCA 1 and ratio image limits the types of lithology found in reality within the area. Because, the Landsat TM sensor can not observe rocks outcropped at cliffs, vertical fault scarps and caldera rims. It has also poor spectral resolution to differentiate the different types of ignimbrites. During field work, additional information concerning the types of rocks in the area are collected in order to complete the map. Therefore, even if satellite images help in tracing accurately lithologic contacts, without the support of field data the resulting photo-geological map and associated analyses is incomplete.

The oldest pyroclastic deposits of the eastern escarpment in the area are faulted by the NE-SW faults which have defined the rift margin. This shows that the rift margin faults were developed after the deposition of the plateau pyroclastics. However, the source of the pyroclastics is not yet clear. They are thought to be of fissural type. Deep fissures are usually rooted on the pre-existing deeper weak zones in the crust such as shear zones (Smith and Mosely, 1993). The recent phases of tectonics in the rift have controlled the spatial distribution and types of associated volcanism. The type of volcanism is mainly related to the depth of faulting, associated fracturing, the geometry of faults with respect to the maximum extension direction (δ_3) and the density of faults.

CONCLUSION

The different stages of the volcano-tectonic events in the concerned area are generalised as follows:

1. Pyroclastics of the plateau are extruded from the first plateau fissures and caldera volcanoes.

2. The marginal escarpment came into being by a major phase of NE-SW faulting which has cut and exposed the escarpment pyroclastics.

3. The reactivation of NW-SE trans-rift faults as transfer faults.

4. Eruption of calderas at the intersections of the trans-rift structures and the major NE-SW faults, and outpouring of the porphyritic basalt of transitional nature.

5. Third major phase of faulting forming the narrow rift-in-rift structures within the rift (WFB).

6. Extrusion of the younger and evolved basalt, rhyolite and obsidian flows through the deep fractures and faults related to WFB.

7. The latest phase of N-S to NNE-SSW faulting that has cut through the volcanic rocks extruded through the fractures linked to the Wonji Faults Belt.

Lithologic mapping using only satellite imagery has certain drawbacks. Nevertheless, by integrating remote sensing and conventional techniques of mapping reasonably accurate results can be obtained. The contribution of satellite imagery in identifying subtle lithologic contacts and tracing regional lineaments which cannot be easily detected by detailed field mapping is appreciable.

Reconnaissance geological mapping in the inaccessible regions of Ethiopia particularly where rocks and their weathered equivalents are exposed, and where vegetation cover is not dense, applying methods of remote sensing is of utmost importance. Large areas can be mapped at scales larger than 1:100,000 in relatively short time, minimum cost and better accuracy.

ACKNOWLEDGEMENTS

I gratefully acknowledge the laboratory of remote sensing, structural geology and geomorphology at the University of Pierre and Marie Curie in Paris where a substantial part of the image processing was done, and the Department of Geology and Geophysics in the Addis Ababa University for facilitating field work. I am grateful to the anonymous reviewers of *SINET* whose suggestions and comments improved the quality of the manuscript and its presentation.

REFERENCE

1. Best, G.M. (1986). *Igneous and Metamorphic Petrology.* CBS publishers and distributers press, 630 pp.

2. Black, R., Morton, W.H. and Rex, D.E. (1975). Block tilting and volcanism within the Afar in the light of recent K/Ar age data. In: *Afar Depression of Ethiopia*, pp. 296–300, (Pilgar, A., and Rosler, S.A., eds). Schweizerbart, Stuttgart, West Germany.

3. Chessex, R., Delaloye, M., Muller, J. and Weidmann, M. (1975). Evolution of the volcanic region of Ali Sabieh (Djibouti) in the light of K/Ar age determinations. In: *Afar Depression of Ethiopia*, pp. 221–227, (Pilgar, A., and Rosler, S.A., eds). Schweizerbart, Stuttgart, West Germany.

4. Chorowicz, J., Collet, B., Bonavia, F. and Tesfaye Korme (1994). Northwest to north-northwest extension direction in the Ethiopian rift deduced from the orientation of extension structures and fault-slip analysis. *Geol. Soci. of Amer. Bull.* **105**:1560–1570.

5. Davidson, A. and Rex, D. (1980). Age of volcanism and rifting in southwestern Ethiopia. *Nature* **283**:657–658.

6. Di Paola, G. (1977). Geological map of the Tullu Moye volcanic area. *Consiglio Naz. Ricerche, Firenze* (map, 1:75,000).

7. Drury, S.A. (1992). A Guide to Remote Sensing Interpreting Images of the Earth. Oxford University Press, 199 pp.

8. Gidey Wolde-Gabriel, Aronson, J.L. and Walter, R.C. (1990). Geology, geochronology and rift basin development in the central sector of the Main Ethiopian Rift. *Geol. Soci. of Amer. Bull.* **102**:439–452.

9. Gupta, R.P. (1977). Delineation of active faulting and tectonic interpretations in Munich-Milan section of eastern Alps - use of Landsat imagery. *Tectonophysics* **38**:297–315.

10. Gupta, R.P. (1991). Remote sensing geology. Springer-Verlag, Inc., Berlin, Heidelberg, 355 pp.

11. Huchinson, R.W. and Engels, G.G. (1970). Tectonic significance of regional geology and evaporite lithofacies in northeastern Ethiopia. *Roya. Soci. of London Phil. Tran.* **12267**:313–329.

12. Juch, D. (1975). Geology of the Southeastern escarpment of Ethiopia between 39° and 42° long. E. In: *Afar Depression of Ethiopia*, pp. 310–316, (Pilgar, A., and Rosler, S.A., eds). Schweizerbart, Stuttgart, West Germany.

13. Kazmin, V. (1979). Stratigraphy and correlation of volcanic rocks in Ethiopia. *Ethi. Inst. of Geol. Surv. note* **106**:1–26.

14. Kunz, K., Kruzer, H. and Miller, P. (1975). Potassium Argon age determinations of the Trap Basalts of South Eastern Part of Afar. In: *Afar Depression of Ethiopia*, pp. 370–394, (Pilgar, A., and Rosler, S.A., eds). Schweizerbart, Stuttgart, West Germany.

15. Levitte, D., Columba, J. and Mohr, P.A. (1974). Reconnaissance geology of Amaro Horst, southern Ethiopia. *Geol. Soci. of Amer. Bull.* 85:417–422.

16. Meyer, W., Pilgar, A., Rosler, A. and Stets, J. (1975). Tectonic evolution of the northern part of the Main Ethiopian Rift. In: *Afar Depression of Ethiopia*, pp. 352–361, (Pilgar, A., and Rosler, S.A., eds). Schweizerbart, Stuttgart, West Germany.

17. Mohr, P.A. (1967a). Review of the geology of the Simien Mountains. *Bull. of the Geop. Obse.* 10:79–93.

18. Mohr, P.A. (1967b). The Ethiopian rift system. *Bull. of the Geop. Obse.* 11:1–65.

19. Morbidelli, L., Nicoletti, M., Petrucciani, C. and Piccirillo, E.M. (1975). Ethiopian southeastern plateau and related escarpment: K/Ar age of the main volcanic events (MER 8°10' to 9°00' Lat. N.). In: *Afar Depression of Ethiopia*, pp. 352–361, (Pilgar, A., and Rosler, S.A., eds). Schweizerbart, Stuttgart, West Germany.

20. Rothery, D.A. (1984). The role of MSS imagery in mapping the Oman ophiolite. In: *Ophiolites and Oceanic Lithosphere* 13:405–413, (Gass, I.G., Lippard, S.J. and Shelton, A.W., eds). Special Publi. of Geol. Soci. of Lond., London.

21. Smith, M. and Mosely, P. (1993). Crustal heterogeneity and basement influence on the development of the Kenya rift, east Africa. *Tectonics* 12(2):591–606.

22. Story, M. and Congalton, G.R. (1986). Accuracy assessment: A user's perspective. *American Society for Photogrammetry and Remote Sensing, Photogrammetric Engineering and Remote Sensing* 52(3):397–399.

23. Tesfaye Korme, Chorowicz, J., Collet, B. and Bonavia, F.F. (1997). Volcanic vents rooted on extension fractures and their geodynamic implications in the Ethiopian Rift. *Journal of Volcanology and Geothermal Research* 79:205–222.

24. Zanettin, B. and Justlin-Visentin, E. (1974). The volcanic succession in Ethiopia, the volcanics of the Western Afar and Ethiopian Rift margins. *Memoire degli Instituti di Geologia e Mineralogia dell' Universita di Padova* 31:1–19.

25. Zanettin, B., Justin-Visentin, E. Nicoletti, M. and Piccirillo, E.M. (1980). Correlation among Ethiopian volcanic formations with special references to the chronological and stratigraphic problems of the Trap Series. *Academia Nazionale dei Lincei* 47:231–252.